Lipogenesis and innate immunity in hepatocellular carcinoma cells reprogrammed by an isoenzyme switch of hexokinases

Laure Perrin-Cocon[1,†], Pierre-Olivier Vidalain[1,†], Clémence Jacquemin[1], Anne Aublin-Gex[1], Keedrian Olmstead[2], Baptiste Panthu[1,3], Gilles J. P. Rautureau[4], Patrice André[1], Piotr Nyczka[5], Marc-Thorsten Hütt[5], Nivea Amoedo[6], Rodrigue Rossignol[6,7], Fabian Volker Filipp[2,8], Vincent Lotteau[1,*‡] Olivier Diaz[1,*‡]

1- CIRI, Centre International de Recherche en Infectiologie, Univ Lyon, Inserm, U1111, Université Claude Bernard Lyon 1, CNRS, UMR5308, ENS de Lyon, 21 Avenue Tony Garnier, F-69007, Lyon, France.

2- Cancer Systems Biology, Institute of Computational Biology, Helmholtz Zentrum München, Ingolstädter Landstraße 1, D-85764, München, Germany.

3- Actual address: Univ Lyon, CarMeN Laboratory, Inserm, INRA, INSA Lyon, Université Claude Bernard Lyon 1, F-69921, Oullins Cedex, France.

4- Université de Lyon, CNRS, Université Claude Bernard Lyon 1, ENS de Lyon, Centre de RMN à Très Hauts Champs (CRMN), FRE 2034, F-69100 Villeurbanne, France.

5- Department of Life Sciences and Chemistry, Jacobs University, Bremen, Germany.

6- CELLOMET, Centre de Génomique Fonctionnelle de Bordeaux, 146 Rue Léo Saignat, F-33000 Bordeaux, France.

7- Univ. Bordeaux, Inserm, MRGM, U1211, F-33076, Bordeaux, France.

8- School of Life Sciences Weihenstephan, Technical University München, Maximus-von-Imhof-Forum 3, D-85354, Freising, Germany.

*** Corresponding authors:**

vincent.lotteau@inserm.fr

olivier.diaz@inserm.fr

† These authors contributed equally to this work

‡These authors jointly supervised this work

Keywords: hepatocellular carcinoma, hexokinase, lipogenesis, innate immunity, lipoproteins

Abstract

Hexokinases catalyse the first step of glycolysis by phosphorylating glucose. In the liver, normal hepatocytes express the low-affinity hexokinase 4, also known as glucokinase (GCK), which is adapting hepatocyte function to glycaemia. Conversely, hepatocellular carcinoma (HCC) cells express the high-affinity hexokinase 2 (HK2) to sustain tumour proliferation even at low glucose concentrations. The analysis of transcriptomic data from human HCC tumours shows that GCK and HK2 expression levels are inversely correlated and associated with patient survival. To explore functional consequences of such a *GCK*-to-*HK2* isoenzyme switch, *HK2* was knocked-out in the HCC cell line Huh7 and replaced by *GCK*. Transcriptomic, metabolomic and immunological profiling revealed that beyond glycolysis, the hexokinase isoenzyme switch rewires central carbon metabolism, promotes lipogenesis, enhances immune functions and restores sensitivity to NK cells. Altogether, our results suggest that the *GCK*-to-*HK2* isoenzyme switch is playing a key role in HCC dedifferentiation and immune escape.

Hepatocellular carcinoma (HCC) is the most common liver cancer and the fourth leading cause of cancer-related death[1]. HCC is closely linked to chronic liver inflammation, chronic hepatitis B or C virus infection, exposure to toxins, and metabolic dysfunction such as non-alcoholic steatohepatitis (NASH). HCC is of poor prognosis, and treatments are essentially based on surgical resection, liver transplantation or aggressive chemo and/or radiotherapy. In patients with advanced HCC, broad-spectrum kinase inhibitors are approved[2] but with limited benefit[3]. Effective personalized therapies are thus needed but their development is impeded by our incomplete understanding of the molecular mechanisms underlying HCC onset and progression. Efforts to characterize the disease on basis of aetiology and outcomes revealed metabolic dysregulation as a hallmark of HCC-subtypes progression[4]. Indeed, metabolic remodelling is critically required for tumour growth as energy demand and anabolic needs drastically increase. In HCC tumours, the Warburg effect is a frequent feature, characterized by excessive glycolytic activity in the presence of oxygen and rewired oxidative phosphorylation[5,6]. Furthermore, such a re-balanced energy metabolism up-regulates the synthesis of biomolecular precursors to support cellular proliferation[7].

Another metabolic feature of HCC cells is impaired lipoprotein biosynthesis. *In vivo*, hepatocytes secrete triglyceride-rich lipoproteins in the form of very-low-density lipoproteins (VLDL) which are modified in the circulation to generate low-density-lipoproteins (LDL) for cholesterol distribution. This highly specialized function is acquired during hepatocyte differentiation but is lost in HCC cells, which can only secrete LDL-like lipoproteins, indicating a defective lipogenesis and/or lipoprotein assembly[8].

Metabolic reprogramming in cancer cells involves the modulation of several enzymes mediated by oncogenic drivers[6]. Targeting these enzymes is now considered as a therapeutic strategy for several types of cancers[6]. Among these enzymes, hexokinase 2 (HK2) stands out

because of its elevated or induced expression in numerous cancers, including HCC[9]. Hexokinases control the first rate-limiting step of glucose catabolism by phosphorylating glucose to glucose-6-phosphate (G6P), fuelling glycolysis as well as glycogen, pentose phosphate and triglyceride synthesis. The human genome contains four genes encoding distinct hexokinase isoenzymes, named HK1 to HK4 (HK4 is also known as glucokinase or GCK), with distinct enzymatic kinetics and tissue distributions. A fifth putative hexokinase enzyme was recently discovered but has not yet been fully characterized[10]. A switch from GCK to HK2 isoenzymes is occurring during the transition from primary to tumour hepatocytes so that HCC cell lines express HK2 but no longer GCK. HK2 expression level has been correlated with disease progression and dedifferentiation of HCC cells[11]. When HK2 is artificially knocked-down in HCC cell lines, glycolysis is repressed, and tumorigenesis is inhibited while cell death increases[9]. In addition, a recent discovery that hexokinase function extends beyond metabolism towards autophagy, cell migration, and immunity suggests that the *GCK*-to-*HK2* isoenzyme switch may have a broader spectrum of functional consequences than initially suspected [12–15]. In the present study, we analysed transcriptomic data of HCC biopsies and correlated hexokinase isoenzyme expression level with overall patient survival. This led us to generate a new HCC human cell line expressing GCK instead of HK2. A comparative analysis of GCK^+ *vs* $HK2^+$ HCC cell lines provided a unique opportunity to look into HK isoenzyme-dependent metabolic features, lipoprotein production and resistance to immune signals of liver cancer cells.

Results

Relative expression level of GCK and HK2 stratifies HCC patients

HK2 expression in hepatocytes is strongly associated with hepatocellular malignancy. Although the isoenzyme switch from GCK to HK2 is supposed to be an early event of the carcinogenesis process[16], the relative expression of hexokinase isoenzymes in the tumours is unclear. We first analysed the transcriptomes (RNAseq data) of 365 HCC biopsies from The Cancer Genome Atlas (TCGA) database[17,18]. All tumours were positive for HK1, whereas 348, 362 and 172 were positive for HK2, HK3, and GCK, respectively. Kaplan-Meyer curves show that HK1 or HK3 expression level does not correlate with the patients' survival rate (Fig. 1A). In contrast, high expression of HK2 and low expression of GCK in the tumours both correlate with a lower overall survival rate. Analysis of this dataset showed that HK2 expression is inversely correlated with GCK expression, suggesting a mutually exclusive setting of HK2 and GCK expression (Fig. 1B and Supplementary table 1). A few patients have an exclusive HK2 profile (*i.e.* 47 patients, 12.9%) whereas the large majority shows a gradation of the GCK/HK2 expression ratio. These data indicate that expression of GCK or HK2 in HCC tumours is strongly associated with clinical outcome.

Engineering a cellular model of the hexokinase isoenzyme switch

To decipher the functional consequences of GCK or HK2 expression in a cancerous hepatocyte, we restored GCK expression by lentiviral transduction in the reference HCC cell line Huh7, and knocked-out the endogenous HK2 gene by CRISPR/Cas9. The exclusive expression of HK2 and GCK in Huh7 and Huh7-*GCK*$^{+}$*/HK2*$^{-}$ cell lines, respectively, was validated (Fig. 2A). The hexokinase activity in the presence of increasing concentration of glucose was determined in protein lysates from the two cell lines. Hexokinase activity in

Huh7 lysate reached its maximum at low glucose concentration, presenting a standard Michaelis–Menten saturation curve (Fig. 2B). The hexokinase activity in Huh7-*GCK*$^{+}$*/HK2*$^{-}$ lysates followed the expected pseudo-allosteric response to glucose[19,20]. Thus, the expected HK2 and GCK activities were observed in the Huh7 and Huh7-*GCK*$^{+}$*/HK2*$^{-}$ cells respectively. We then compared the new Huh7-*GCK*$^{+}$*/HK2*$^{-}$ and the parental Huh7 cell lines (*i.e.* Huh7-*GCK*$^{-}$*/HK2*$^{+}$) at a transcriptomic, metabolic and immunological level.

Cellular movement and lipid metabolism distinguish Huh7 and Huh7-*GCK*$^{+}$*/HK2*$^{-}$

Transcriptomic profiles of Huh7 and Huh7-*GCK*$^{+}$*/HK2*$^{-}$ cells were determined by next generation sequencing (Supplementary table 2). Overall, 4.3% of the genes were transcriptionally reduced and 6% were induced in Huh7-*GCK*$^{+}$*/HK2*$^{-}$ compared to Huh7 (Fig. 2C; |fold-change|>2 and adjusted *p*-value<0.05). Enrichment of molecular and cellular functions in differentially expressed genes using Ingenuity Pathway Analysis revealed that cellular movement and lipid metabolism are the most affected functions (Fig. 2D and Supplementary table 3). A closer look at these annotations pointed to differences in the migratory capacities (Fig. 2E) as well as lipid concentration and synthesis (Fig. 2F). The migratory capacities of Huh7 and Huh7-*GCK*$^{+}$*/HK2*$^{-}$ were compared using transwell-migration cell assays (Fig. 2G). Results showed a higher migratory capacity of Huh7-*GCK*$^{+}$*/HK2*$^{-}$ cells, in line with the report of Kishore M. et al showing that GCK expression induced by pro-migratory signals controls the trafficking of Treg cells[15]

To validate the differences in lipid metabolism highlighted by the transcriptomic analysis, intracellular content in neutral lipids was determined upon labelling with lipophilic dyes. As assessed by Oil Red O staining, an accumulation of intracellular lipid droplets containing neutral lipids is observed in Huh7-*GCK*$^{+}$*/HK2*$^{-}$ in comparison to Huh7 (Fig. 2I). This was

confirmed and quantified after BODIPY staining of intracellular neutral lipids and flow cytometry analysis (Fig. 2J). Therefore, the hexokinase isoenzyme switch resulted in lipid droplets accumulation in Huh7-*GCK*$^{+}$*/HK2*$^{-}$ cells.

Differential lipid metabolism in Huh7 and Huh7-*GCK*$^{+}$*/HK2*$^{-}$

The intracellular lipid content of the two cell lines was further analysed. In Huh7-*GCK*$^{+}$*/HK2*$^{-}$, an enrichment in phosphatidylcholine, cholesterol, triglycerides (TG) and free fatty acids was observed compared to Huh7 (Fig. 3A). One major function of hepatocytes is to secrete triglyceride-rich VLDL and this function is altered in HCC cells that secrete smaller lipoproteins with the density of LDL[21,22]. The secretion of lipids and lipoproteins by both cell lines was analysed after a 24h-culture in the absence of foetal calf serum to exclude any participation of exogenous lipids in the production of lipoproteins. Huh7-*GCK*$^{+}$*/HK2*$^{-}$ secreted more free fatty acids than Huh7 while secretion of cholesterol and TG remained unchanged (Fig. 3B). However, under the same conditions, the secretion of apolipoprotein B (ApoB) by Huh7-*GCK*$^{+}$*/HK2*$^{-}$ was reduced compared to Huh7. Since ApoB is a non-exchangeable protein with only one copy in VLDL and LDL particles, an elevated TG/ApoB ratio indicates that ApoB^{+}-lipoproteins secreted by Huh7-*GCK*$^{+}$*/HK2*$^{-}$ cells are enriched in TG compared to lipoproteins secreted by Huh7 (Fig. 3C). This was confirmed by the ApoB distribution in density gradient fractions showing a secretion of ApoB^{+}-LDL by Huh7 and ApoB^{+}-VLDL by Huh7-*GCK*$^{+}$*/HK2*$^{-}$ (Fig. 3D). As hepatocytes *in vivo* secrete VLDL and not LDL, this indicates that GCK expression is essential for VLDL assembly/secretion pathway and could explain the loss of this crucial metabolic pathway in hepatoma cells expressing HK2 instead of GCK[23].

Differential activity of the tricarboxylic acid cycle (TCA) in Huh7 and Huh7-*GCK*$^{+}$*/HK2*$^{-}$

We observed that GCK expression induced lipogenesis, resulting in intracellular accumulation of lipid droplets and secretion of VLDL. A rewiring of cellular metabolism towards energy storage in Huh7-*GCK*$^{+}$/*HK2*$^{-}$ was thus suspected and confirmed by the accumulation of glycogen, creatinine and creatinine-P (Fig. 4A and B), a feature of functional hepatocytes. To determine the consequences of replacing HK2 by GCK on the metabolome, we quantified prominent intracellular metabolites via gas chromatography-mass spectrometry. Figure 4C shows relative intracellular quantities of metabolites that are significantly different between Huh7 and Huh7-*GCK*$^{+}$/*HK2*$^{-}$. Higher levels of glucose and lactic acid were detected in Huh7-*GCK*$^{+}$/*HK2*$^{-}$. Among differentially represented metabolites, we identified several intermediates of the TCA cycle (succinic acid, fumaric acid, alpha-ketoglutaric acid), and metabolites directly connected to it (GABA, glutamic acid, glutamine, aspartic acid). This supports a significant modulation of central carbon metabolism by the HK isoenzyme switch at the level of both glycolysis and the TCA cycle. Other metabolic pathways were also modified such as nucleoside/nucleotide metabolism as assessed by changes in uracil, thymine, adenosine, adenine and 2-deoxyribose-5-phosphate levels. Higher intracellular creatinine was confirmed in cells expressing GCK. Interestingly, glycerol-3-phosphate, an intermediate of phospholipids and TG biosynthesis, was also increased in Huh7-*GCK*$^{+}$/*HK2*$^{-}$, in line with TG and phosphatidylcholine accumulation (Fig. 3A) and an activated lipogenesis pathway.

Pyruvate entering the mitochondria downstream of glycolysis can be either oxidized by pyruvate dehydrogenase (PDH), producing acetyl-CoA, or converted into oxaloacetate (OAA) by pyruvate carboxylase (PC). Acetyl-CoA and OAA are then combined in the TCA cycle to form citrate. *De novo* lipogenesis requires citrate egress from the TCA cycle to serve as a precursor of cytosolic acetyl-CoA for further synthesis of fatty acids. In Huh7-*GCK*$^{+}$/*HK2*$^{-}$ cells,

we observed both an increased activity of PC (Fig. 4D) without changes in protein expression (Fig. 4E) and an increased phosphorylation of pyruvate dehydrogenase (PDH), which is indicative of a reduced activity of this enzyme (Fig. 4F). This is consistent with the increased expression of the PDH kinase PDK2 and the decreased expression of the PDH phosphatase PDP2 in Huh7-*GCK*$^{+}$*/HK2*$^{-}$ cells that regulate the PDH phosphorylation state (Fig. 4G). A rebalanced usage of pyruvate in Huh7-*GCK*$^{+}$*/HK2*$^{-}$ cells maintains a functional TCA cycle and supports lipogenesis. In Huh7-*GCK*$^{+}$*/HK2*$^{-}$ cells, we also observed an increased phosphorylation of ATP citrate lyase (ACLY), the first enzyme of the fatty acid synthesis pathway, indicating an enhanced activity of this enzyme (Fig. 4H). This reaction also regenerates OAA in the cytosolic compartment. Interestingly, transcriptomic data show that PCK1 which converts OAA to PEP, a precursor of glycerol-3-phosphate for TG synthesis, is expressed in Huh7-*GCK*$^{+}$*/HK2*$^{-}$cells whereas it is absent in Huh7.

The shift in pyruvate oxidation to carboxylation is observed in cancer cells where succinate dehydrogenase (SDH) is inactivated by mutation and OAA can only be generated through PC activity[24]. SDH inhibition leads to succinate accumulation, especially in activated immune cells[25]. Interestingly, higher levels of succinate were measured in Huh7-*GCK*$^{+}$*/HK2*$^{-}$ cells compared to Huh7 (Fig. 4I), pointing to a reduced activity of SDH. This was confirmed when measuring SDH enzymatic activity in Huh7-*GCK*$^{+}$*/HK2*$^{-}$ (Fig. 4J). Even though SDH is also part of the complex II of the mitochondrial respiratory chain, we observed that oxygen consumption is increased in Huh7-*GCK*$^{+}$*/HK2*$^{-}$ (Fig. 4K), suggesting that other pathways maintain a high activity of the respiratory chain by fuelling complex III. Thereby, the HK isoenzyme switch rewired the TCA cycle promoting carboxylation of pyruvate into OAA in the presence of a reduced SDH activity.

Gene-centric metabolic analysis of transcriptomic data revealed extended modifications of metabolic connections

The metabolic consequences of the HK isoenzyme switch can also be determined from the transcriptome profiles by mapping the differentially expressed genes onto reference metabolic networks and extracting highly-connected subgraphs (see Methods and Supplementary Figure 1-4). Recon2 and HepatoNet1, two well-established bipartite metabolic networks connecting gene products and metabolites, were used as framework[26]. Highest-degree metabolites were first removed as currency metabolites, and each network was simplified by bipartite network projection to obtain gene-centric networks (*i.e.* without metabolites) and transcriptomic data were used to filter these gene-centric networks. The optimal expression fold-change was set according to the best connectivity score obtained for the resulting subgraphs (see Methods and Supplementary Fig. 1-4). Clusters of genes that are both differentially expressed and connected by common metabolites emerge from this analysis, thus highlighting metabolic modules that distinguish Huh7 from Huh7-*GCK*$^{+}$/*HK2*$^{-}$. Interestingly, we found that across a wide range of analysis parameters, including varying rates of currency metabolites and gene expression fold-change, the differentially expressed genes are substantially better connected in the HepatoNet1 metabolic model of liver cells than in the generic human metabolic model Recon2 (Supplementary Fig. 4). This highlights the specificity of the transcriptomic changes with respect to hepatocyte metabolism. To obtain the spanned network presented in Fig. 5, we applied to the liver model HepatoNet1 an optimal fold-change threshold of 2 for transcriptomic data and removed 5 percent of highest-degree currency metabolites (thus retaining 95 percent of metabolites in the network). The effective network spanned by the differentially expressed genes shows connected components within and between lipid metabolic clusters, reinforcing our above

data, but also hexoses, nucleotides and amino acids pathways. It also shows modifications in gene expression amongst the connected clusters pyruvate/malate, mevalonate, one-carbon pathways and urea cycle. This analysis highlights the global impact of the HK isoenzyme switch that spreads way beyond glycolysis and across distant connected metabolic modules.

Restored immune sensitivity in Huh7-*GCK*$^{+}$/*HK2*$^{-}$

Lipid accumulation in hepatocytes is incriminated in hepatic inflammation[27] and TCA cycle rewiring is associated with innate immunity activation[28]. These two events were observed when replacing HK2 by GCK in Huh7 cells, questioning the immune status of these cells and their sensitivity to antitumour immunity. By analysing transcriptomic data with the GO term "Type I-IFN signalling pathway", we observed that amongst the 91 genes of this GO term, 17 were significantly up-regulated (FC>2, BH p<0.05) in Huh7-*GCK*$^{+}$/*HK2*$^{-}$ compared to Huh7 (Fig. 6A). This includes IRF1, 7 and 9, three crucial transcription factors, IFN-stimulated genes (ISGs) including Mx1, OAS1, OAS3 and signalling intermediates such as IKBKE (IKKε gene) (Fig. 6B). The expression of the RIG-like receptor (RLR) MDA5 (IFIH1 gene) was slightly higher in Huh7-*GCK*$^{+}$/*HK2*$^{-}$ whereas that of RIG-I was unchanged. These results suggested that Huh7-*GCK*$^{+}$/*HK2*$^{-}$ cells may be better equipped than Huh7 cells to respond to immune signals. We thus compared the immune response of the two cell lines when stimulated by ligands of RIG-I and MDA5, two members of the RLR family involved in immune sensing and antitumor defence[29]. RIG-I and MDA5 were activated by transfection with triphosphate-hairpin RNA (3p-hpRNA) and poly(I:C), respectively. Induction of the innate immune response was first monitored using an ISRE-luciferase reporter gene. ISRE-dependent transcription was efficiently induced by RLR ligands in Huh7-*GCK*$^{+}$/*HK2*$^{-}$ cells whereas Huh7 response was very limited even at high doses of ligands (Fig. 6C).

To investigate whether this differential sensitivity to RLR ligands is linked to GCK expression or HK2 knockout, we used Huh7-derived cells transduced for GCK expression so that they express both HK2 and GCK (Huh7-*GCK*$^{+}$/*HK2*$^{+}$). In these cells, the response to RIG-I ligation did not differ from that of Huh7 cells suggesting that GCK expression alone is not sufficient to restore immune sensitivity and pointing towards HK2 as a negative regulator of RLR signalling (Fig. 6D). When HK2 expression was repressed in these cells with a shRNA (Huh7-*GCK*$^{+}$/*HK2*$^{-}$Sh) (see Supplementary Fig. 5 showing 95% extinction of HK2 protein), ISRE response to RIG-I signalling was restored to a level similar to that observed in Huh7-*GCK*$^{+}$/*HK2*$^{-}$ cells (Fig. 6D). This indicates that HK2 expression is inhibiting the RIG-I response in HCC cells and strongly suggests that the *GCK*-to-*HK2* isoenzyme switch during malignant transformation of hepatocytes is accompanied by a reduced sensitivity to immune signals that could favour escape to immune surveillance. The higher sensitivity to RLR ligands of Huh7-*GCK*$^{+}$/*HK2*$^{-}$ cells also resulted in increased secretion of inflammatory (IL-6 and IL-8) and antiviral cytokines (IFN-λ_1, IFN-$\lambda_{2/3}$, IFN-β and IP-10) (Fig. 6E), indicating that it induced both NF-κB and IRF3 dependent signalling pathways. IL-1β, TNFα, IL-12p70, GM-CSF, IL-10 and IFNγ were not detected in the supernatants of none of the cell lines, whether they were stimulated or not.

As NK cell-mediated lysis of tumour cells is crucial for the anti-cancer immune defence, we compared the susceptibility of the two cell lines to NK cells cytotoxicity. Primary NK cells purified from the blood of healthy donors were co-cultured with Huh7 and Huh7-*GCK*$^{+}$/*HK2*$^{-}$ cells for 4 h and cell death was monitored by flow cytometry analysis after morphological gating on hepatocytes. Figure 6F shows that Huh7 cells are resistant to NK cell-mediated lysis. However, replacing HK2 by GCK restored Huh7 sensitivity to NK cell-mediated lysis. Similar results were obtained when NK cells were pre-activated with IL-2 (cf. Supplementary

Fig. 6). Altogether, these results demonstrate that HCC cells expressing HK2 instead of GCK exhibit an impaired response to immune signals and also a strong resistance to NK cells. Significantly, these two observations are in line with clinical data showing that elevated GCK expression is associated with prolonged survival, while elevated HK2 expression coinciding with GCK depletion correlates with shorter overall survival (Fig. 1).

Discussion

Metabolic network rewiring is a hallmark of cancer although for most tumours, mechanisms at the origin of this metabolic reprogramming have not been elucidated. While GCK, but not HK2, is expressed in normal hepatocytes, the expression of HK2 occurs during cirrhosis and increases as the disease progresses to carcinoma[16]. Analysing TCGA data from human HCC tumours, we observed that HK2 and GCK expression is inversely correlated and that high HK2/GCK ratio is of poor prognosis. On the contrary, HK1 and HK3 expression levels were not correlated to patient survival. As HK2 and GCK expression tend to be mutually exclusive, both HK2 induction and GCK downregulation might have consequences on the metabolic reprogramming during malignant transformation of hepatocytes. To compare the functional consequences of the HK isoenzyme switch in HCC, we therefore expressed GCK in the reference HCC cell line Huh7 and knocked-down HK2 expression. Our comparative transcriptomic, metabolic and functional studies demonstrate that the replacement of HK2 by GCK not only restored some essential metabolic functions of normal hepatocytes such as lipogenesis, VLDL secretion and glycogen storage but also reactivated innate immune responses and sensitivity to NK lysis.

HCC cell lines predominantly secrete LDL-like particles, unlike normal hepatocytes that secrete TG-enriched VLDL. Lipid loading of Huh7 cells with oleic acid can boost the secretion of $ApoB^+$ particles but does not induce a shift from LDL to VLDL density, indicating that intracellular fatty acid accumulation of exogenous origin cannot rescue VLDL production[23]. Here we show that replacing HK2 by GCK in Huh7 cells restored *de novo* fatty acid synthesis, allowing VLDL assembly/secretion in the absence of exogenous lipids. To our knowledge Huh7-*GCK^+/$HK2^-$* is the first human cell line with a functional VLDL secretion pathway that

should strongly benefit the field of lipoprotein-associated cardiovascular diseases and hepatic steatosis.

De novo fatty acid synthesis from carbohydrates requires an adequate supply in metabolic substrates, especially citrate produced by the TCA cycle which is exported out of the mitochondria. The glycolytic entry point into the TCA cycle is controlled by PDH and PC that convert pyruvate into acetyl-CoA or OAA, respectively. Our data revealed that PC activity is increased in contrast to PDH that is inhibited, suggesting that pyruvate metabolism is rebalanced in favour of OAA in Huh7-*GCK*$^{+}$/*HK2*$^{-}$ cells, as described in healthy liver. Such a mechanism of anaplerosis is known to replenish TCA cycle intermediates and compensate citrate export out of the mitochondria to fuel lipogenesis. Increased PC activity is observed in both normal and pathological situations, mainly as a result of an increased transcription of the PC gene. In our model, mRNA and protein levels were not affected, indicating that PC activity can be regulated by alternative mechanisms depending on HK isoenzyme expression.

A rebalanced pyruvate usage in favour of OAA is also described for instance for SDH-deficient neuroendocrine tumour cells, where succinate accumulates and PC activity is increased to maintain OAA production, replenish the oxidative TCA cycle and support aspartate synthesis[24]. Interestingly, in comparison to Huh7 cells, succinate and aspartate levels are elevated in Huh7-*GCK*$^{+}$/*HK2*$^{-}$ where SDH activity is reduced, suggesting a direct link between PC and SDH activity in hepatocytes depending on HK isoenzyme expression.

Several mechanisms inhibiting SDH have been described[30]. Modification of the expression of SDH subunits is unlikely as no variation was observed at the transcriptomic level. Itaconate is a weak inhibitor of SDH produced by IRG1 from aconitate but this metabolite was not detected and IRG1 mRNA was absent from the transcriptome of both cell lines. Whether

fumarate or other metabolites are responsible for the reduced SDH activity in GCK-expressing cells remains to be further investigated.

SDH-deficient cells and LPS-Stimulated macrophages have been shown to elicit a hypoxic-like phenotype through accumulation of large amounts of succinate and stabilization of HIF-1α[31,32] . Despite an elevated succinate steady-state level in Huh7-*GCK*$^{+}$*/HK2*$^{-}$ compared to Huh7 cells, we observed no difference in HIF-1α stabilization neither at basal level nor upon induction (Supplementary Fig. 7). This suggested that while the reduction of SDH activity in Huh7-*GCK*$^{+}$*/HK2*$^{-}$ cells was observed, this reduction was not strong enough to induce a pseudo-hypoxic phenotype. Overall our data indicate that when GCK replaced HK2 in Huh7, cells adapted to the HK isoenzyme switch by rewiring their metabolism, resulting in a metabolic profile resembling to some extend that of normal hepatocytes.

Our gene-centric metabolic analysis of transcriptomic data revealed a wide spreading of metabolic modifications resulting from HK isoenzyme switch. Illustrating these modifications, figure 7 is an attempt to integrate the observed changes in central carbon metabolism and closely connected metabolic pathways. In particular, decreased levels of alanine and increased aspartate concentrations in Huh7-*GCK*$^{+}$*/HK2*$^{-}$ cells could be an indirect effect of PC activation that uses pyruvate for the synthesis of OAA. As a consequence, hepatic transaminases may balance intracellular pools of OAA, aspartate, alanine and pyruvate. Glutamate and GABA levels were also modified, thus supporting anaplerosis of the TCA cycle through glutamine consumption and the GABA shunt pathway, respectively. We also observed lower levels of oxalate, an end-product of glyoxylate degradation. Increased levels of the enzyme AGXT (serine-pyruvate aminotransferase) could account for this phenotype as it converts alanine and glyoxylate into pyruvate and glycine which is increased. Interestingly, high levels of AGXT is a good prognostic marker for HCC[33]. We also observed

that isoleucine and valine levels increased while the expression of BCAT1 (Branched Chain Amino Acid Transaminase 1) decreased. This suggests a reduced catabolism of branched chain amino acids in Huh7-*GCK*$^{+}$/*HK2*$^{-}$ cells. Again, low levels of BCAT1 is a good prognostic marker for HCC and oral supplementation with branched chain amino acids has been shown to reduce the risk of liver cancer in cirrhotic patients[34,35]. If some metabolic modifications seem to advocate for a normal hepatocyte phenotype restoration following the replacement of HK2 by GCK, it cannot be a general statement. Indeed, the urea cycle was also impacted in Huh7-*GCK*$^{+}$/*HK2*$^{-}$ cells with lower levels of CPS1 and OTC, which are also observed in aggressive HCC tumours[36]. Altogether, our results demonstrate the broad impact of replacing HK2 by GCK in HCC cells, and the key role played by the HK isoenzyme switch in HCC tumour metabolism.

Most importantly, we discovered that HK isoenzyme expression not only controls hepatic metabolic functions but also interferes with intrinsic innate immunity of hepatocytes and antitumoral immune surveillance. Several reports have recently established functional links between glucose metabolism and signaling pathways downstream of innate immunity sensors of the RLR family, RIG-I and MDA5[37–39], which are usually associated with antiviral responses. However, RIG-I expression is downregulated in hepatic cancer tissues and low RIG-I expression is correlated with poor survival of patients, whereas RIG-I expression in HCC cell lines enhanced IFN response and cancer cell apoptosis[29]. This suggests an unexpected role of this receptor family in the antitumoral response. Here we show that Huh7 cells expressing GCK instead of HK2 exhibit a higher sensitivity to RIG-I and MDA5 ligands, and produce higher levels of type I/III IFNs and inflammatory cytokines. Interestingly, it has been shown recently that glucose metabolism, which drives not only glycolysis but also the hexosamine biosynthetic pathway, promotes MAVS signalling through the generation of

UDP-GlcNAc[37]. This metabolite is crucial to the O-GlcNAcylation and activation of MAVS, the mitochondrial signalling adaptor downstream RIG-I and MDA5[37]. Thus, an intriguing hypothesis is that GCK expression could increase MAVS signalling ability by upregulating the hexosamine biosynthetic pathway. HK2 binding at the surface of mitochondria may also compete with pyruvate carboxylase, metabolites or mitochondria factors known to control MAVS signalling[37–39]. Further investigations are now required to decipher the molecular mechanisms involved.

Beyond the inhibition of RLR signalling, other mechanisms might contribute to tumour escape from immune surveillance in HCC patients. In advanced-stage HCC patients, NK cells often exhibit reduced infiltration and impaired functional activities[40]. We thus compared the sensitivity of Huh7-*GCK*$^{+}$*/HK2*$^{-}$ cells to Huh7, and found that sensitivity to NK cell lysis is unlocked when HK2 is replaced by GCK. When analysing cell surface expression of HLA class I molecules and MICA/B, no significant changes were observed between cell lines (cf. Supplementary Fig. 6). In contrast, an increased ICAM-1 transcription and surface expression (FC = 2.6; cf. Supplementary Fig. 6) were observed in Huh7-*GCK*$^{+}$*/HK2*$^{-}$. Since ICAM-1 binding to active LFA-1 at the surface of NK cells is essential for granule polarization and efficient killing of the target cells[41], its enhanced exposition at the surface of Huh7-*GCK*$^{+}$*/HK2*$^{-}$ may contribute to their higher sensitivity to NK cell-mediated killing. These results suggest that HK2 expression at the expense of GCK in HCC tumours decreases immune responsiveness and sensitivity to NK cytotoxicity, thus favouring immune escape. Overall our data indicate that HK2 and GCK isoenzymes play a crucial role in establishing the metabolic and immune status of hepatocytes during their malignant transformation.

Methods

Cell generation and culture. Cells were cultured at 37°C and 5% CO_2 in Dulbecco's Modified Eagle's Medium (DMEM; Life Technologies) containing 10% foetal calf serum (FCS; Dominique Dutcher, Brumath, France), penicillin/streptomycin and supplemented with 1.0 mM pyruvate, 2.0 mM L-glutamine and 25 mM glucose. The different cell lines were generated starting from Huh7 cells. 15.10^4 cells were transduced for GCK expression at different MOIs (lentiviral transduction using pLEX-GCK construct). The Huh7-*GCK*$^+$/*HK2*$^+$ cells were then cultured for 7 days in the presence of puromycin at 1 µg/mL before amplification and freezing for storage.

Abrogation of HK2 expression was performed using CRISPR/Cas9 system as previously described[42] to obtain Huh7-*GCK*$^+$/*HK2*$^-$. A single guide RNA (sgRNA) pair was designed for double nicking using the online CRISPR Design Tool (http://tools.genome-engineering.org). The guide sequence oligos (sgRNA$_1$(*HK2*): 5'-CACCGTGACCACATTGCCGAATGCC-3' and sgRNA$_2$(*HK2*): 5'-CACCGTTACCTCGTCTAGTTTAGTC-3') were cloned into a plasmid containing sequences for Cas9 expression and the sgRNA scaffold (pSpCas9(BB)-2A-GFP, Addgene plasmid #48138). 48 h post-transfection, transfected cells were sorted by flow cytometry based on the transient expression of GFP from the pSpCas9(BB)-2A-GFP vector. Cloning by limiting dilution from GFP-positive cells was used to obtain a clonal cell line. Effective deletion of HK2 was assessed by qPCR.

HK2 extinction was alternatively obtained from Huh7-*GCK*$^+$/*HK2*$^+$ cells after lentiviral transduction of HK2-targeting shRNA and selection of transduced cells with 100 µg/ml hygromycin. The sequence targeting *HK2* (5'-CCGGCCAGAAGACATTAGAGCATCTCTCGAGAGATGCTCTAATGTCTTCTGGTTTTTT-3' was cloned in the pLKO.1 hygro vector, a gift from Bob Weinberg (Addgene plasmid #24150). HK2

expression in Huh7-*GCK*$^{+}$/*HK2*$^{+}$ and Huh7-*GCK*$^{+}$/*HK2*$^{-}$*Sh* was analysed on cell lysates by western blotting (Supplementary Fig. 5).

Hexokinase activity assay. The method used for extracting HK from cells was adapted from Kuang et al.[43], and the assay was a modification of that previously described[44,45]. Cellular pellets stored at -80°C were thawed and immediately homogenized (100 µl/2.10^{6} cells) in precooled buffer (Tris–HCl, 0.05 M; sucrose, 0.25 M; EDTA, 0.005 M (pH 7.4); 2-mercaptoethanol, 0.005 M). After 20 min incubation on ice, homogenates were pulse-sonicated 15 s at half power (EpiShear Probe Sonicator). Homogenates were then centrifuged at 500 g for 20 min at 4°C. Supernatants were immediately used for determination of HK activity, which was measured spectrophotometrically through NADP+ reduction in the glucose 6-phosphate dehydrogenase–coupled reaction. HK activity was assayed in medium containing 50 mM triethanolamine (pH = 7.6), 10 mM $MgCl_2$, 1.4 mM NADP+, with variable concentration of glucose and 1U glucose 6-phosphate dehydrogenase (*S. cerevisiae*), equilibrated to 37°C. The reaction was started by addition of ATP (final concentration 1.9 mM), and absorbance was continuously recorded for 30 min at 340 nm (TECAN Infinite M200, Lyon, France).

Pyruvate Carboxylase activity assay. The method used for quantification of PC activity was adapted from Payne et al.[46]. Briefly, cells were centrifuged, washed twice with ice-cold PBS before homogenisation in Tris-HCL 100 mM, pH 8.0 using a Dounce homogenizer. Homogenates were pulse-sonicated 15 s at half power (EpiShear Probe Sonicator) before centrifugation at 500 g for 5 min. Supernatants were immediately used for the assay. PC activity was assayed in medium containing 100 mM Tris-HCl, 50 mM $NaHCO_3$, 5 mM $MgCl_2$, 0.1 mM Acetyl-CoA, 0.25 mM 6,6'-Dinitro-3,3'-dithiodibenzoic acid (DTNB), 5 mM ATP, 5 mM pyruvate, citrate synthase and cofactors. Reduction of DTNB by the generated free CoA was

measured continuously by Abs at 412 nm and recorded for 30 min (TECAN Infinite M200, Lyon, France). The same assay was performed in absence of pyruvate to subtract background signal.

Metabolomics profiling of HCC model cells. For metabolomics profiling, cells were seeded at 13.10^5 cells per 75 cm^2 dishes. After 24 h, culture media was replaced and cells were further incubated during 24 h. Cells were harvested, washed twice with ice-cold PBS and cell pellets were frozen at -80°C until metabolites extraction. Cell pellets were transferred into a pre-chilled microcentrifuge tube with 1 mL cold extraction buffer consisting of 50% methanol (A452, Fisher Scientific, Fair Lawn, NJ) in ultrapure water with 20 µM L-norvaline (N7627, Millipore Sigma) and 20 µM DL-norleucine (N1398, Millipore Sigma). Samples were then frozen in liquid nitrogen, thawed, and placed in a shaking dry bath (Thermo Fisher Scientific, Waltham, MA) set to 1100 rpm for 15 min at 4 °C. After centrifugation for 15 min at 12500 g and 4°C (Sorvall, Thermo Fisher Scientific, Waltham, MA) using a fixed-angle F21-48x1.5 rotor, supernatants were collected and dried by vacuum centrifugation overnight. Dried metabolites were derivatized by addition of 20 µL of 2.0% methoxyamine-hydrochloride in pyridine (MOX, TS-45950, Thermo Fisher Scientific) followed by incubation during 90 min in shaking dry bath at 30 °C and 1100 rpm. Ninety µL of N-methyl-N-(trimethylsilyltrifluoroacetamide (MSTFA, 701270.201, Macherey-Nagel, Düren, Germany) was added, and samples were incubated and shaken at 37 °C for 30 min before centrifugation for 5 min at 14,000 rpm and 4 °C. Metabolites contained in the supernatant were then separated by gas chromatography (GC, TRACE 1310, Thermo Fisher Scientific) coupled to a triple-quadrupole mass spectrometry system for analysis (QQQ GCMS, TSQ8000EI, TSQ8140403, Thermo Fisher Scientific), equipped with a 0.25 mm inner diameter, 0.25 µm film thickness, 30 m length 5% diphenyl/95% dimethyl polysiloxane

capillary column (OPTIMA 5 MS Accent, 725820.30, Macherey-Nagel) and run under electron ionization at 70 eV. Using established separation methods[47–49], the GC was programed with an injection temperature of 250.0 °C and splitless injection volume of 1.0 µL. The GC oven temperature program started at 50 °C (323.15 K) for 1 min, rising at 10 K/min to 300.0 °C (573.15 K) with a final hold at this temperature for 6 min. The GC flow rate with helium carrier gas (HE, HE 5.0UHP, Praxair, Danbury, CT) was 1.2 mL/min. The transfer line temperature was set at 290.0 °C and ion source temperature at 295.0 °C. A range of 50-600 m/z was scanned with a scan time of 0.25 s.

Metabolomics data processing. Metabolites were identified using TraceFinder (v3.3, Thermo Fisher Scientific) based on libraries of metabolite retention times and fragmentation patterns (Metaflux, Merced, CA). Identified metabolites were quantified using the selected ion count peak area for specific mass ions, and standard curves generated from reference standards run in parallel. Peak intensities were median normalized and adjusted for extraction efficiency using L-norvaline as an internal standard. The mean and standard deviation for each quantified metabolite was calculated for each cell line and treatment condition. A univariate t-test was used to compare treatment conditions for each metabolite and cell line.

Transcriptome profiling of Huh7 and Huh7-*GCK*$^{+}$/*HK2*$^{-}$ cell lines. Total RNA was extracted and purified from cell pellets using Direct-zol RNA purification kit (Zymo Research, Tustin, CA). 700 ng of total RNA were amplified (NextFlex Rapid Directional mRNA-Seq, PerkinElmer, Courtaboeuf, France) to generate mRNA-seq libraries. Then, gene expression was analysed by Next-Generation Sequencing (NGS) using Illumina NextSeq500. Reads were mapped on the reference genome Homo sapiens GRCh37/hg19 using Tophat v2.1.0. Signals were normalized using cufflinks[50] v2.1.1 which use FPKM (fragments per kilobases of exon per

million mapped reads) method. Counted reads were analysed for differential expression of genes between Huh7 and Huh7-*GCK*$^{+}$*/HK2*$^{-}$ cell lines using Student's t-test with Benjamini-Hochberg correction. See supporting information and Gene Expression Omnibus database with the accession number GSE144214 for entire raw data.

Pathway analysis. The list of gene transcripts differentially expressed in Huh7 and Huh7-*GCK*$^{+}$*/HK2*$^{-}$ cell lines was analysed by gene set enrichment analysis (IPA, Build version: 486617M, Qiagen, Aarhus, Denmark) weighted by their corresponding fold change and *p*-value. The fold change cut-off of median expression for each transcript FPKM was set at 2 with a *p*-value<0.05. Differentially expressed transcripts were included in the analysis and the highest represented molecular and cellular functions were obtained with their detailed functional annotations and the related *p*-value. The list of genes associated with "Type I-IFN signalling pathway" was defined in the AmiGO 2 database. The gene FPKM (sum of the transcript FPKMs) expression data of these genes were retrieved from transcriptomes of Huh7-*GCK*$^{+}$*/HK2*$^{-}$ and Huh7.

Cell migration assay. Transwell migration assay was performed as follow. Cells were seeded at 2.10^4 and plated in the upper chamber with DMEM without FCS to allow migration for 24 h at 37°C. DMEM with 10 % FCS complementation was distributed in each well, below the chamber. Chambers were gently picked up before a brief PBS rinse and 0.05 % crystal violet coloration. Cells at the bottom position of the chamber were photographed and counted with a binocular loop (Leica microsystems).

Respiration Assay. Five hours prior measuring respiration in the Seahorse Extracellular Flux Analyzer, the cells were seeded in XF 96-well cell culture microplates (Seahorse Bioscience) at 5.10^4 cells/well in 100 µL of DMEM medium supplemented with 10 mM HEPES and 10% FCS (Gibco 11885084), and then incubated at 37°C/5% CO_2 during 5 h for cells attachment.

The assay was initiated by removing the growth medium from each well and replacing it with 160 µL of Seahorse assay medium (sigma D5030 + 5 mM Glucose, 2 mM Glutamine and 1 mM sodium pyruvate) prewarmed at 37°C. Cells were incubated at 37°C for 30 min to allow media temperature and pH to reach equilibrium before the first rate measurement. The oxygen consumption rate (OCR) was measured using the following Seahorse running program: injection Port A - 1 µM Oligomycin; Injection port B - 1 µM CCCP and injection port C – 0.5 µM Rotenone/Antimycin A. The number of cells was determined at the end of the run using the SRB assay as described by Skehan *et al*.[51].

Intracellular lipid staining. For fluorescence microscopy staining of intracellular lipids, cells were seeded and cultured during 48 h before staining. Cells were washed with PBS before fixation with a 4% formaldehyde solution, during 15 min at RT. Cells were then washed twice with water before incubation during 5 min with isopropanol 60%. Isopropanol was then removed and Oil Red O solution (Millipore Sigma-Aldrich, Saint-Quentin Fallavier, France) added on cells for 15 min at RT. Cells were then extensively washed with water to remove the exceeding dye before nucleus counterstaining with NucBlue Fixed Cell Stain ReadyProbes reagent (ThermoFisher Scientific, Villebon sur Yvette, France) and observation with a Nikon Eclipse Ts2R microscope. For the quantification of intracellular lipid droplets by flow-cytometry, cells were stained with the BODIPY® 493/503 dye (Tocris Bio-Techne, Rennes, France) after 48 h of culture. The cells were washed with PBS before being incubated for 5 min with a 5 µM BODIPY® solution in PBS at 37°C. Cells were then washed with PBS before trypsination and FACS analysis. A 7-AAD (BioLegend, London, United Kingdom) staining of dead cells, prior to FACS analysis, allowed gating on living cells.

Protein, ApoB, and Lipid Quantification. Protein concentration was determined using Coomassie Plus (Bradford) Protein assay (BioRad, Marnes-la-Coquette, France). ApoB

concentration in medium and gradients fractions was determined via specific ELISA as described previously[52]. Total concentrations of cholesterol, phospholipids, and triglycerides (TG) were determined using specific assays (Millipore Sigma-Aldrich, Saint-Quentin Fallavier, France). Free Fatty Acids were quantified using specific assay kit (Abcam, Cambridge, United Kingdom).

Iodixanol density gradients. Iodixanol gradients were prepared as previously described[53]. Gradients were precast in thin-wall centrifuge tubes (14x89 mm, Beckman) using a two-chamber gradient maker. One ml of culture supernatant was applied to the top of 6 to 56% iodixanol gradients and centrifuged for 10 h in a Beckman Optima L100 XP ultracentrifuge at 41,000 rpm and 4°C in a SW41 rotor. The gradient was harvested by tube puncture from the bottom and collected into 22 fractions (0.5 ml each). The density of each fraction was determined by weighing (balance of precision, Sartorius).

Metabolic network coherence computational analysis. In order to measure the agreement of a set of differentially expressed genes with a metabolic network, we employed the metabolic network coherence measure introduced by Sonnenschein *et al.*[54] and applied to various disease-related transcriptome profiles in Sonnenschein *et al.*[55] and Knecht *et al.*[56]. It has also served as a mean of extracting information on the genetic control of metabolic organization[57]. We first extracted a gene-centric metabolic network from a given genome-scale metabolic model. This was achieved via the stoichiometric matrix and the gene-reaction associations contained in the metabolic model. We constructed the two projections of the bipartite graph represented by the stoichiometric matrix, yielding a metabolite-centric and a reaction-centric graph. The metabolite-centric graph allowed us to identify high-degree nodes ('currency metabolites' like H_2O, ATP, etc.), which are not informative about the network-like organization of the metabolic systems and need to be eliminated before

interpreting the network architecture (see[58] and[55] for details). The degree of a node is the number of neighbours the node has in the network. The percentage of remaining metabolites is one of the parameters of our analysis. Typical values are 90 to 98 percent (*i.e.* a removal of the highest 2 to 10% of metabolites with the highest degree as currency metabolites). After recomputing the reaction-centric graph based on the reduced number of metabolites (see Supplementary Fig. 1), we can now evaluate the gene-reaction associations to arrive at a gene-centric metabolic network (see Supplementary Fig. 2 and 3). Given a set *S* of differentially expressed genes and the gene-centric metabolic network *G*, we can now analyse the subgraph of *G* spanned by all genes in *S*. The percentage *c* of connected nodes in these subgraphs serves as a measure of the connectivity of this subgraph (see Supplementary Fig. 2). The metabolic network coherence *MC* is the z-score of *c* computed with respect to a null model of randomly drawn gene sets with the same size as *S*. In this way, *MC* has an intuitive interpretation: The value of *MC* indicates, how many standard deviations away from randomness the connectivity of the subgraph spanned by the observed gene set *S* actually is (see Supplementary Fig. 4 and ref.[59]). The genome-scale metabolic models employed here are the generic human metabolic model Recon 2[60] and the metabolic model of a liver cell, HepatoNet 1[26].

Western-Blot Analysis. Proteins were extracted from 10^6 cells by incubation on ice for 15 min in lysis buffer (1% Triton X-100 and 5 mM EDTA in PBS) containing 1% protease inhibitor cocktail (P8340; Millipore Sigma-Aldrich, Saint-Quentin Fallavier, France) followed by centrifugation at 12,000 rpm during 20min. For phosphorylation analysis 2 mM orthovanadate was added in lysis buffer. Supernatants were diluted in Laemmli buffer and heated at 95°C during 5 min prior to fractionation by SDS-PAGE and transfer to a PVDF membrane. After saturation in PBS-0.1% Tween 20 supplemented with 5% (w/v) non-fat milk

powder, blots were incubated 1 h at room temperature with primary antibody in PBS-0.1% Tween 20 (1:2,000 dilution). Incubation with secondary antibody was performed after washing for 1 h at room temperature. HRP-labelled anti-goat (sc-2020, Santa Cruz Biotechnology), anti-rabbit (A0545, Millipore Sigma-Aldrich) or anti-mouse (115-035-174, Jackson ImmunoResearch Laboratories) antibodies were diluted 20,000 folds and detected by enhanced chemiluminescence reagents according to the manufacturer's instructions (SuperSignal Chemiluminescent Substrate, Thermo Fisher Scientific). Primary antibodies used for immunoblotting included mouse mAb against human GCK (clone G-6, sc-17819, Santa Cruz Biotechnology), rabbit mAb against human HK2 (Clone C64G5, #2867, Cell Signaling Technology), goat pAb against human ACLY (SAB2500845, Millipore Sigma-Aldrich), rabbit pAb against human pACLY (phospho S455, #4331 Cell Signaling Technology), rabbit mAb against human PDH (C54G1, #3205, Cell Signaling Technology), rabbit mAb against human pPDH E1-alpha subunit (phospho S293, ab92696, Abcam), goat pAb against human PC (SAB2500845, Millipore Sigma-Aldrich).

RLR stimulation

Cells were seeded in 96 well white-plates (12,000/100 µl) or 24 well plates (80,000/500 µl) 24 h before transfection for the specified doses of the RIG-I specific ligand 3p-hpRNA or the MDA5/TLR3 ligand high molecular weight poly(I:C) (both from Invivogen) with the reporter plasmids pISRE-luc (1.25 µg/ml) and pRL-SV40 (0.125 µg/ml) and JetPEI-Hepatocyte reagent (Polyplus Transfection, Illkirch, France) according to the manufacturer instructions. After 48 h, supernatants were collected for cytokines assays and ISRE-dependent firefly luciferase and constitutive Renilla luciferase expressions were successively quantified using Dual-Glo luciferase Assay system (Promega, Charbonnières-les-bains, France) and luminescence was read by Infinite M200 microplate reader (TECAN, Lyon, France).

Cytokine assays

Clarified culture supernatants were collected after treatment and stored at -20°C. IL-8 was assayed using quantitative cytokine-specific Cytometric Bead Array Flex Sets (BD Biosciences, Le Pont de Claix, France). The other cytokines were assayed using human LEGENDPlex multiplex assays allowing simultaneous quantification of IL-1β, IL-6, IL-8, IL-10, IL-12p70, IFN-α_2, IFN-β, IFN-λ_1, IFN-$\lambda_{2/3}$, IFN-γ, TNF-α, IP-10 and GM-CSF (BioLegend). Fluorescence was analysed using FACS Canto II flow cytometer (BD Biosciences).

NK cell cytotoxicity test

NK cells were isolated from human buffy coats of healthy donors, obtained from the Etablissement Français du Sang. All experiments were performed in accordance with the guidelines of the World Medical Association's Declaration of Helsinki. Experimental procedures were approved by the local institutional review committee. PBMCs were isolated by standard density gradient centrifugation on Ficoll-Hypaque (Eurobio, Courtaboeuf, France). Mononuclear cells were separated from peripheral blood lymphocytes (PBLs) by centrifugation on a 50% Percoll solution (GE Healthcare, Velizy, France). NK cells were purified from PBLs by immunomagnetic depletion using pan-mouse IgG Dynabeads (Thermo Fisher Scientific) with a cocktail of depleting mAbs: anti-CD19 (4G7 hybridoma), anti-CD3 (OKT3 hybridoma, ATCC, Manassas, VA, USA), anti-CD4, anti-CD14 and anti-glycophorin A (all from Beckman Coulter, Villepinte, France). NK purity was >70% as assessed by CD56 labelling (data not shown).

Huh7 or Huh7-*GCK*$^+$/*HK2*$^-$ were seeded at 1.10^5 cells per well in a 24 well-plate, 24 h prior to addition of 3.10^5 or 3.10^6 NK cells, in RPMI 1640 with 10% FCS and 40 µg/ml gentamycin. The cytotoxicity assay was performed for 4 h at 37°C, under 5% CO_2. Target hepatoma cells were harvested after trypsination, labelled with propidium iodide (PI) and analysed by flow

cytometry. The percentage of lysis was given by the percentage of PI^+ cells after gating on large hepatoma cells.

Statistics and reproducibility

All the statistical analyses were performed in GraphPad Prism or Analyse-it softwares. In general, *p*-values<0.05 was considered statistically significant and specific *p*-values are indicated directly in Figures. The details of methods used for statistical analyses can be found in each figure legend. Experiments were repeated at least three times.

Data availability

The datasets that support the findings of this study are available from the corresponding author upon request. DNA-sequence of GCK and RNA-sequence datasets of Huh7 and Huh7-*GCK*$^+$*/HK2*$^-$ cell lines used in this study were deposited in the Gene Expression Omnibus database with the accession number GSE144214.

References

1. Villanueva, A. Hepatocellular Carcinoma. *N. Engl. J. Med.* **380**, 1450–1462 (2019).
2. Kudo, M. *et al.* Lenvatinib versus sorafenib in first-line treatment of patients with unresectable hepatocellular carcinoma: a randomised phase 3 non-inferiority trial. *The Lancet* **391**, 1163–1173 (2018).
3. Llovet, J. M., Montal, R., Sia, D. & Finn, R. S. Molecular therapies and precision medicine for hepatocellular carcinoma. *Nat. Rev. Clin. Oncol.* **15**, 599–616 (2018).
4. De Matteis, S. *et al.* Aberrant Metabolism in Hepatocellular Carcinoma Provides Diagnostic and Therapeutic Opportunities. *Oxid. Med. Cell. Longev.* **2018**, 1–13 (2018).
5. Filipp, F. V. *et al.* Glutamine-fueled mitochondrial metabolism is decoupled from glycolysis in melanoma. *Pigment Cell Melanoma Res.* **25**, 732–739 (2012).

6. Hay, N. Reprogramming glucose metabolism in cancer: can it be exploited for cancer therapy? *Nat. Rev. Cancer* **16**, 635–649 (2016).

7. Vander Heiden, M. G., Cantley, L. C. & Thompson, C. B. Understanding the Warburg effect: the metabolic requirements of cell proliferation. *Science* **324**, 1029–1033 (2009).

8. Jiang, J., Nilsson-Ehle, P. & Xu, N. Influence of liver cancer on lipid and lipoprotein metabolism. *Lipids Health Dis.* **5**, 4 (2006).

9. DeWaal, D. *et al.* Hexokinase-2 depletion inhibits glycolysis and induces oxidative phosphorylation in hepatocellular carcinoma and sensitizes to metformin. *Nat. Commun.* **9**, 446 (2018).

10. Guo, C. *et al.* Coordinated regulatory variation associated with gestational hyperglycaemia regulates expression of the novel hexokinase HKDC1. *Nat. Commun.* **6**, 6069 (2015).

11. Guzman, G. *et al.* Evidence for Heightened Hexokinase II Immunoexpression in Hepatocyte Dysplasia and Hepatocellular Carcinoma. *Dig. Dis. Sci.* **60**, 420–426 (2015).

12. Wolf, A. J. *et al.* Hexokinase Is an Innate Immune Receptor for the Detection of Bacterial Peptidoglycan. *Cell* **166**, 624–636 (2016).

13. Tan, V. P. & Miyamoto, S. HK2/hexokinase-II integrates glycolysis and autophagy to confer cellular protection. *Autophagy* **11**, 963–964 (2015).

14. Roberts, D. J., Tan-Sah, V. P., Ding, E. Y., Smith, J. M. & Miyamoto, S. Hexokinase-II Positively Regulates Glucose Starvation-Induced Autophagy through TORC1 Inhibition. *Mol. Cell* **53**, 521–533 (2014).

15. Kishore, M. *et al.* Regulatory T Cell Migration Is Dependent on Glucokinase-Mediated Glycolysis. *Immunity* **47**, 875-889.e10 (2017).

16. Lee, N. C. W., Carella, M. A., Papa, S. & Bubici, C. High Expression of Glycolytic Genes in Cirrhosis Correlates With the Risk of Developing Liver Cancer. *Front. Cell Dev. Biol.* **6**, 138 (2018).

17. Uhlén, M. *et al.* Tissue-based map of the human proteome. *Science* **347**, (2015).

18. Uhlen, M. *et al.* A pathology atlas of the human cancer transcriptome. *Science* **357**, (2017).

19. Porter, C. M. & Miller, B. G. Cooperativity in monomeric enzymes with single ligand-binding sites. *Bioorganic Chem.* **43**, 44–50 (2012).

20. Larion, M., Salinas, R. K., Bruschweiler-Li, L., Miller, B. G. & Brüschweiler, R. Order–Disorder Transitions Govern Kinetic Cooperativity and Allostery of Monomeric Human Glucokinase. *PLoS Biol.* **10**, e1001452 (2012).

21. Berghe, G. van den. The role of the liver in metabolic homeostasis: Implications for inborn errors of metabolism. *J. Inherit. Metab. Dis.* **14**, 407–420 (1991).

22. Berg, J. M., Tymoczko, J. L. & Stryer, L. Each Organ Has a Unique Metabolic Profile. *Biochem. 5th Ed.* (2002).

23. Meex, S. J. R., Andreo, U., Sparks, J. D. & Fisher, E. A. Huh-7 or HepG2 cells: which is the better model for studying human apolipoprotein-B100 assembly and secretion? *J. Lipid Res.* **52**, 152–158 (2011).

24. Lussey-Lepoutre, C. *et al.* Loss of succinate dehydrogenase activity results in dependency on pyruvate carboxylation for cellular anabolism. *Nat. Commun.* **6**, 8784 (2015).

25. Lampropoulou, V. *et al.* Itaconate Links Inhibition of Succinate Dehydrogenase with Macrophage Metabolic Remodeling and Regulation of Inflammation. *Cell Metab.* **24**, 158–166 (2016).

26. Gille, C. *et al.* HepatoNet1: a comprehensive metabolic reconstruction of the human hepatocyte for the analysis of liver physiology. *Mol. Syst. Biol.* **6**, 411 (2010).

27. Mansouri, A., Gattolliat, C.-H. & Asselah, T. Mitochondrial Dysfunction and Signaling in Chronic Liver Diseases. *Gastroenterology* **155**, 629–647 (2018).

28. Mills, E. L., Kelly, B. & O'Neill, L. A. J. Mitochondria are the powerhouses of immunity. *Nat. Immunol.* **18**, 488 (2017).

29. Hou, J. *et al.* Hepatic RIG-I predicts survival and interferon-α therapeutic response in hepatocellular carcinoma. *Cancer Cell* **25**, 49–63 (2014).

30. Van den Bossche, J., O'Neill, L. A. & Menon, D. Macrophage Immunometabolism: Where Are We (Going)? *Trends Immunol.* **38**, 395–406 (2017).

31. Tannahill, G. M. *et al.* Succinate is an inflammatory signal that induces IL-1β through HIF-1α. *Nature* **496**, 238–242 (2013).

32. Kluckova, K. & Tennant, D. A. Metabolic implications of hypoxia and pseudohypoxia in pheochromocytoma and paraganglioma. *Cell Tissue Res.* **372**, 367–378 (2018).

33. Sun, Y. *et al.* Loss of alanine-glyoxylate and serine-pyruvate aminotransferase expression accelerated the progression of hepatocellular carcinoma and predicted poor prognosis. *J. Transl. Med.* **17**, 390 (2019).

34. Muto, Y. *et al.* Overweight and obesity increase the risk for liver cancer in patients with liver cirrhosis and long-term oral supplementation with branched-chain amino acid granules inhibits liver carcinogenesis in heavier patients with liver cirrhosis. *Hepatol. Res.* **35**, 204–214 (2006).

35. Kawaguchi, T. *et al.* Branched-chain amino acids prevent hepatocarcinogenesis and prolong survival of patients with cirrhosis. *Clin. Gastroenterol. Hepatol.* **12**, 1012-1018.e1 (2014).

36. Ally, A. *et al.* Comprehensive and Integrative Genomic Characterization of Hepatocellular Carcinoma. *Cell* **169**, 1327-1341.e23 (2017).

37. Li, T. *et al.* O-GlcNAc Transferase Links Glucose Metabolism to MAVS-Mediated Antiviral Innate Immunity. *Cell Host Microbe* **24**, 791-803.e6 (2018).

38. Zhang, W. *et al.* Lactate Is a Natural Suppressor of RLR Signaling by Targeting MAVS. *Cell* **178**, 176-189.e15 (2019).

39. Cao, Z. *et al.* Pyruvate Carboxylase Activates the RIG-I-like Receptor-Mediated Antiviral Immune Response by Targeting the MAVS signalosome. *Sci. Rep.* **6**, 22002 (2016).

40. Cai, L. *et al.* Functional impairment in circulating and intrahepatic NK cells and relative mechanism in hepatocellular carcinoma patients. *Clin. Immunol.* **129**, 428–437 (2008).

41. Bryceson, Y. T., March, M. E., Barber, D. F., Ljunggren, H.-G. & Long, E. O. Cytolytic granule polarization and degranulation controlled by different receptors in resting NK cells. *J. Exp. Med.* **202**, 1001–1012 (2005).

42. Ran, F. A. *et al.* Genome engineering using the CRISPR-Cas9 system. *Nat. Protoc.* **8**, 2281–2308 (2013).

43. Kuang, Y., Schomisch, S. J., Chandramouli, V. & Lee, Z. Hexokinase and glucose-6-phosphatase activity in woodchuck model of hepatitis virus-induced hepatocellular carcinoma. *Comp. Biochem. Physiol. C Toxicol. Pharmacol.* **143**, 225–231 (2006).

44. Ramière, C. *et al.* Activity of hexokinase is increased by its interaction with hepatitis C virus protein NS5A. *J. Virol.* **88**, 3246–3254 (2014).

45. Perrin-Cocon, L. *et al.* Toll-like Receptor 4-Induced Glycolytic Burst in Human Monocyte-Derived Dendritic Cells Results from p38-Dependent Stabilization of HIF-1α and Increased Hexokinase II Expression. *J. Immunol.* **201**, 1510–1521 (2018).

46. Payne, J. & Morris, J. G. Pyruvate carboxylase in Rhodopseudomonas spheroides. *J. Gen. Microbiol.* **59**, 97–101 (1969).

47. Lanning, N. J. *et al.* Metabolic profiling of triple-negative breast cancer cells reveals metabolic vulnerabilities. *Cancer Metab.* **5**, 6 (2017).

48. Shah, R., Singh, S. J., Eddy, K., Filipp, F. V. & Chen, S. Concurrent Targeting of Glutaminolysis and Metabotropic Glutamate Receptor 1 (GRM1) Reduces Glutamate Bioavailability in GRM1+ Melanoma. *Cancer Res.* **79**, 1799–1809 (2019).

49. Filipp, F. V., Scott, D. A., Ronai, Z. A., Osterman, A. L. & Smith, J. W. Reverse TCA cycle flux through isocitrate dehydrogenases 1 and 2 is required for lipogenesis in hypoxic melanoma cells. *Pigment Cell Melanoma Res.* **25**, 375–383 (2012).

50. Trapnell, C. *et al.* Transcript assembly and abundance estimation from RNA-Seq reveals thousands of new transcripts and switching among isoforms. *Nat. Biotechnol.* **28**, 511–515 (2010).

51. Skehan, P. *et al.* New colorimetric cytotoxicity assay for anticancer-drug screening. *J. Natl. Cancer Inst.* **82**, 1107–1112 (1990).

52. Scholtes, C. *et al.* High plasma level of nucleocapsid-free envelope glycoprotein-positive lipoproteins in hepatitis C patients. *Hepatology* **56**, 39–48 (2012).

53. Icard, V. *et al.* Secretion of hepatitis C virus envelope glycoproteins depends on assembly of apolipoprotein B positive lipoproteins. *PloS One* **4**, e4233 (2009).

54. Sonnenschein, N., Geertz, M., Muskhelishvili, G. & Hütt, M.-T. Analog regulation of metabolic demand. *BMC Syst. Biol.* **5**, 40 (2011).

55. Sonnenschein, N. *et al.* A network perspective on metabolic inconsistency. *BMC Syst. Biol.* **6**, 41 (2012).

56. Knecht, C., Fretter, C., Rosenstiel, P., Krawczak, M. & Hütt, M.-T. Distinct metabolic network states manifest in the gene expression profiles of pediatric inflammatory bowel disease patients and controls. *Sci. Rep.* **6**, 32584 (2016).

57. Schlicht, K. *et al.* The metabolic network coherence of human transcriptomes is associated with genetic variation at the cadherin 18 locus. *Hum. Genet.* **138**, 375–388 (2019).

58. Ma, H. & Zeng, A.-P. Reconstruction of metabolic networks from genome data and analysis of their global structure for various organisms. *Bioinformatics* **19**, 270–277 (2003).

59. Hütt, M.-T. Understanding genetic variation - the value of systems biology. *Br. J. Clin. Pharmacol.* **77**, 597–605 (2014).

60. Thiele, I. *et al.* A community-driven global reconstruction of human metabolism. *Nat. Biotechnol.* **31**, 419–425 (2013).

61. Gao, J. *et al.* Integrative Analysis of Complex Cancer Genomics and Clinical Profiles Using the cBioPortal. *Sci. Signal.* **6**, pl1 (2013).

62. Cerami, E. *et al.* The cBio Cancer Genomics Portal: An Open Platform for Exploring Multidimensional Cancer Genomics Data. *Cancer Discov.* **2**, 401–404 (2012).

Declarations

Ethics approval and consent to participate

Not applicable.

Competing interests

There is no competing financial interest.

Funding and acknowledgements

This work was supported by the Fondation pour la Recherche Médicale (FRM), grant number DEQ20160334893 to VL. We thank Marco Binder for Huh7 cells. We acknowledge the contribution of the AniRA-Cytometry and PLATIM-microscopy Core Facilities of SFR Biosciences (UMS3444/US8). We acknowledge the contribution of ProfileXpert, Genomics and Microgenomics platform, University Lyon 1, SFR santé LYON-EST, UCBL-Inserm US 7-CNRS UMS 3453. F.V.F. is grateful for the support by grants CA154887, GM115293, CRN-17-427258, NSF GRFP, and the Science Alliance on Precision Medicine and Cancer Prevention by the German Federal Foreign Office, implemented by the Goethe-Institute, Washington, DC, USA, and supported by the Federation of German Industries (BDI), Berlin, Germany.

Author contributions

L.P-C., P-O.V., O.D., V.L. designed the experiments with critical advices from G.J.P.R., P.A., R.R. and F.V.F.; C.J., A.A-G., K.O., B.P., G.J.P.R., N.A, R.R. and F.V.F. performed experiments and analysed the data; P.N. and M-T.H. performed metabolic network computational

analysis; L.P-C., P-O.V., P.A., F.V.F, V.L. and O.D. analysed the data, prepared figures and wrote the manuscript.

Additional information

Supplementary information is provided with a file of supplementary figures and 3 supplementary tables.

Figure Legends

Fig. 1 Correlation between hexokinase (HK) expression levels in HCC tumours and overall survival of patients. (A) Kaplan–Meier estimates of the overall survival of HCC patients depending on the expression of HK1, HK2, HK3 and GCK (HK4) genes in tumour biopsies (n=365). Optimal stratification between low and high expression groups was determined based on RNA-Seq gene expression data. Cut offs were set at 3.8, 1.4, 0.36, and 0.015 for HK1, HK2, HK3, and GCK, respectively. (B) GCK and HK2 expression levels across HCC biopsies from patients (Data from The Cancer Genome Atlas (TCGA) analysed with cBioPortal[61,62]). Patients were ranked by increasing GCK/HK2 expression ratios. Spearman's correlation test, *p*-value=0.019.

Fig. 2 Hexokinase (HK) isoenzyme switch in Huh7 cells modifies their migration capacity and lipid metabolism. (A) Western-blot analysis of HK2 and GCK expression in Huh7 and Huh7-*GCK+/HK2-*. (B) Hexokinase activity in homogenates of Huh7 and Huh7-$GCK^{+}/HK2^{-}$ cells. (C) Comparison of gene expression patterns in Huh7 and Huh7-$GCK^{+}/HK2^{-}$ cells (see Supplementary table 2 for details). (D) Analysis of differentially expressed genes in the two cell lines using gene set enrichment analysis (|fold change| expression above 2 with an adjusted *p*-value<0.05). Top five enriched molecular and cellular functions are presented. (E) and (F) Ranked IPA-annotations associated with 'cellular movement' and 'lipid metabolism'. (G-H) Results of transwell-migration tests. (G) Representative pictures and (H) count of migrating cells. (I) Oil Red O staining of lipid droplets (in red) with nucleus counterstaining (blue). (J) Quantification of intracellular lipids by flow cytometry after BODIPY staining of cells. H and J correspond to means ± SEM with n≥3 (p-value determined by Student's t-test).

Fig. 3 Lipogenesis and VLDL secretion is restored in Huh7-*GCK*$^{+}$*/HK2*$^{-}$ cells. (A) Quantification of intracellular lipids in total cell extracts of Huh7 and Huh7-*GCK*$^{+}$*HK2*$^{-}$ cells. (B) Lipids and ApoB secretions in supernatants of cells cultured 24h in absence of FCS. (C) TG/ApoB molar ratio calculated from quantifications determined in (B). (D) Whole cell supernatants of Huh7 and Huh7-*GCK*$^{+}$*/HK2*$^{-}$ were analysed by ultracentrifugation on iodixanol density gradients. ApoB was quantified in each fraction by specific ELISA. Presented data correspond to means ± SEM of at least 3 experiments with calculated *p*-values (Student's t-test) except for (D) that shows one representative experiment.

Fig. 4 TCA rewiring after hexokinase isoenzyme switch in Huh7 cells. (A) Quantification of glycogen in whole cell extract of Huh7 and Huh7-*GCK*$^{+}$*/HK2*$^{-}$ cells. (B) Creatinine and creatinine-P quantification in Huh7 and Huh7-*GCK*$^{+}$*/HK2*$^{-}$ cells. (C) Metabolomics profiling identifies rewiring of central carbon metabolism upon hexokinase isoenzyme switch. This bubble plot compares intracellular metabolomes of Huh7 and Huh7-*GCK*$^{+}$/*HK2*$^{-}$ cell lines. Metabolite pool sizes larger in Huh7 are indicated in blue, whereas the one larger in Huh7-*GCK*$^{+}$/*HK2*$^{-}$ are shown in red. The area of bubbles inversely scales with *p*-values between 5.10^{-2} and 1.10^{-17} of significant differential metabolomics responses. (D) Pyruvate carboxylase (PC) activity determined in cell homogenates. (E) Western-blot analysis of PC expression in Huh7 and Huh7-*GCK*$^{+}$*/HK2*$^{-}$ cells. (F) Western-blot analysis of pyruvate dehydrogenase (PDH) E1-alpha subunit phosphorylation at ser293. (G) RNAseq quantification of pyruvate dehydrogenase kinase 2 (PDK2) and pyruvate dehydrogenase phosphatase 2 (PDP2). (H) Western-blot analysis of ATP-citrate Lyase (ACLY) phosphorylation at ser455. (I) Succinate quantification in cell homogenates of Huh7 and Huh7-*GCK*$^{+}$*/HK2*$^{-}$. (J) Succinate dehydrogenase (SDH) activity determined in cell homogenates. (K) Quantification

of oxygen consumption rate (OCR) for Huh7 and Huh7-*GCK*$^{+}$/*HK2*$^{-}$ cells. Data correspond to means ± SEM (n=3).

Fig. 5 Gene-centric analysis of metabolic pathways affected by the hexokinase isoenzyme switch. Clusters of metabolism-associated genes that are either up (red) or downregulated (blue) in Huh7-*GCK*$^{+}$/*HK2*$^{-}$ *vs* Huh7 cells were extracted from transcriptomic data using HepatoNet1 as framework (|FC|>2; *p*-value<0.05). Edges connect cellular genes coding enzymes that have at least one metabolite in common, either as substrate or product. Displayed network was built using the Cytoscape software. Grey areas delimitate clusters of genes belonging to the same metabolic module.

Fig. 6 Huh7-*GCK*$^{+}$/*HK2*$^{-}$ cells are primed to amplify innate immune response. (A-B) Sector chart from the transcriptomic study showing genes included in the GO-term "Type I-IFN signalling pathway". (C) List of 17 genes significantly up-regulated (|FC|>2, BH *p*-value<0.05) in Huh7-*GCK*$^{+}$/*HK2*$^{-}$compared to Huh7 cells. (C-E) Cells were stimulated or not for 48 h with 3p-hpRNA (RIG-I ligand) or poly(I:C) (MDA5 ligand). ISRE-luciferase expression was monitored and normalized to Renilla luciferase (C-D). The conditioned media was assayed for cytokine concentration by multiplex assays. IL-1β, TNFα, IL-12p70, GM-CSF, IL-10 and IFNγ were not detected in none of these supernatants (E). (F) NK cell mediated lysis of Huh7 or Huh7-*GCK*$^{+}$/*HK2*$^{-}$. Hepatoma cells were seeded 24 h before NK cells addition for 4 h at effector to target (E:T) ratio of 0, 3 or 30. After harvesting, cells were stained with propidium iodide and analysed by flow cytometry. Lysis was determined by the percentage of PI^{+} cells on gated hepatocytes. The graph shows box and whiskers with dot plots for 3 experiments.

p-values were obtained from 2-way ANOVA analyses comparing matched cell means with Sidak's correction for multiple comparison, with α=0.05

Fig. 7 Simplified scheme of central carbon metabolism and connected pathways showing differences between Huh7-*GCK*$^{+}$/*HK2*$^{-}$ compared to Huh7. Highlighted metabolites, enzymatic activities, and metabolism-associated genes were selected from metabolomic (Fig. 4C), enzymatic (Fig. 4D-J), and transcriptomic analyses (Fig. 5).

Figure 1

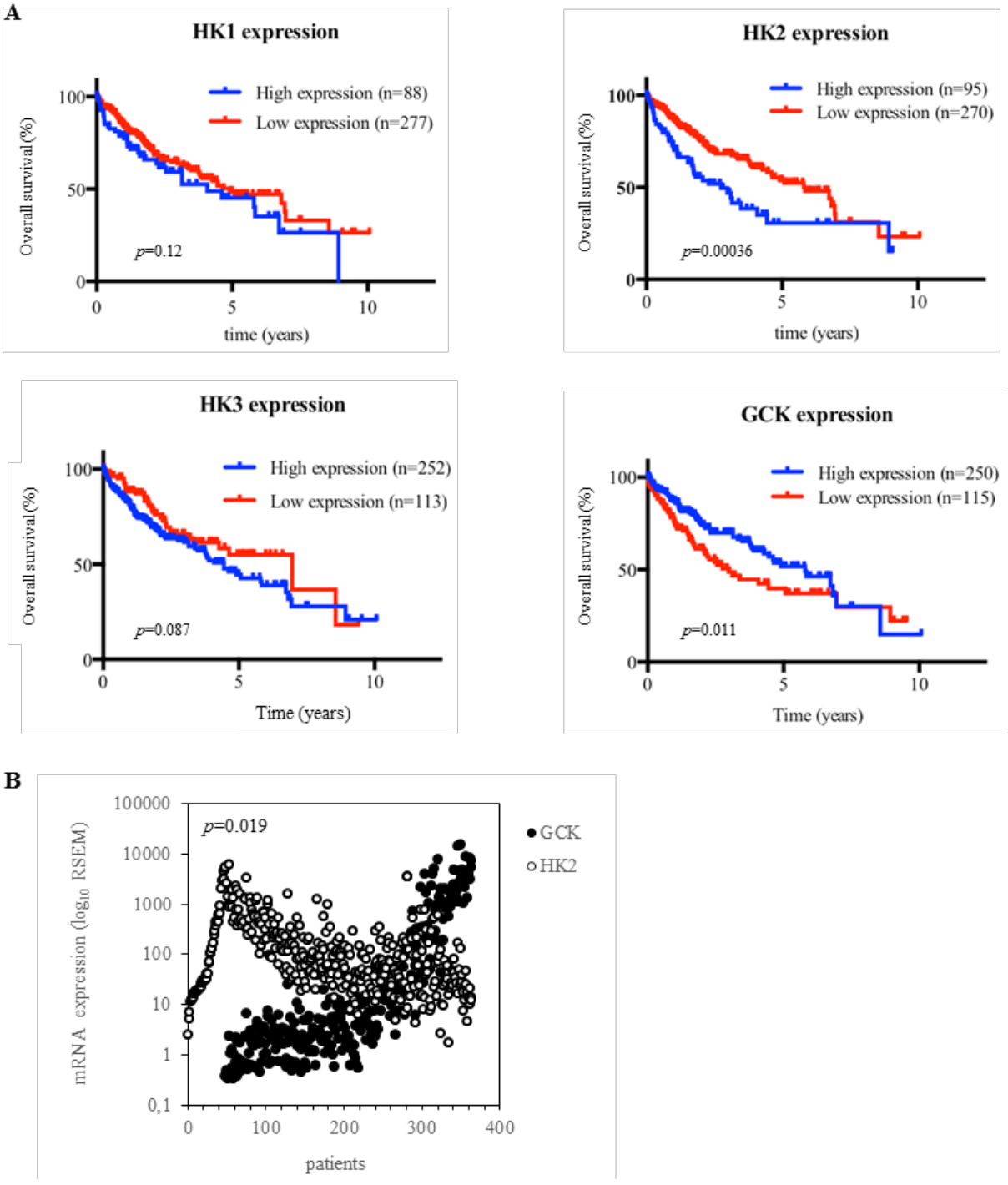

Figure 2

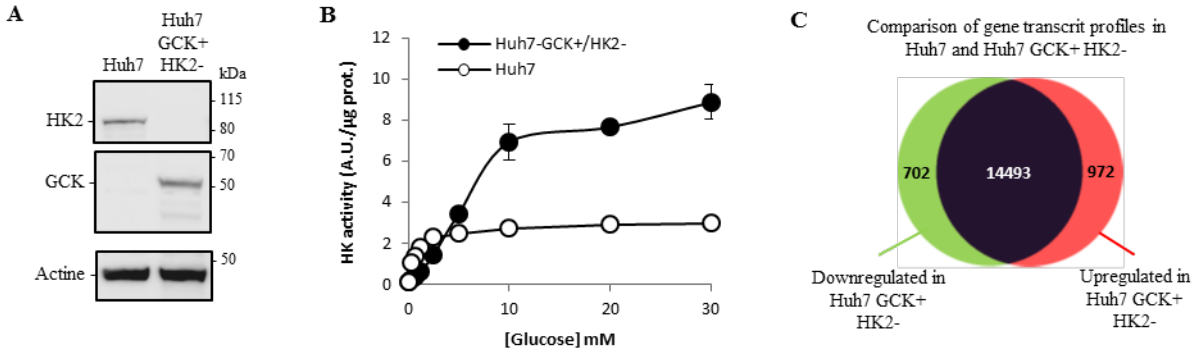

D

Molecular and Cellular Functions		
Name	***p*-value range**	**Number of genes involved**
Cellular Movement	**7.43×10^{-5} - 1.60×10^{-17}**	**463**
Lipid Metabolism	**4.04×10^{-5} - 9.01×10^{-13}**	**277**
Molecular Transport	1.49×10^{-5} - 9.01×10^{-13}	390
Small Molecule Biochemistry	4.04×10^{-5} - 9.01×10^{-13}	321
Cell Death and Survival	7.93×10^{-5} - 7.75×10^{-12}	597

E

Cellular Movement Functional Annotations		
Name	***p*-value**	**Number of genes involved**
Migration of cells	1.60×10^{-17}	397
Cell movement	8.21×10^{-17}	436
Cell movement of tumor cell lines	2.86×10^{-12}	218
Cellular infiltration	6.63×10^{-12}	109
Migration of tumor cell lines	1.05×10^{-11}	186

F

Lipid Metabolism Functional Annotations		
Name	***p*-value**	**Number of genes involved**
Concentration of lipid	9.01×10^{-13}	181
Synthesis of lipid	2.50×10^{-8}	156
Fatty acid metabolism	4.09×10^{-8}	112
Concentration of fatty acid	1.43×10^{-7}	66
Concentration of triacylglycerol	1.50×10^{-7}	74

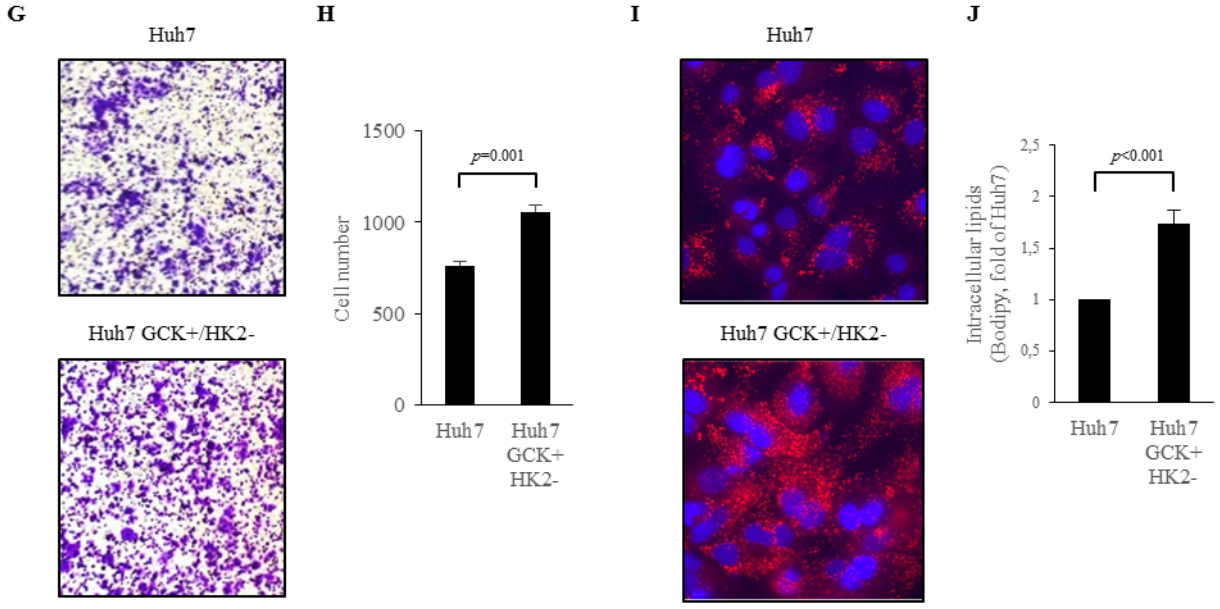

Figure 3

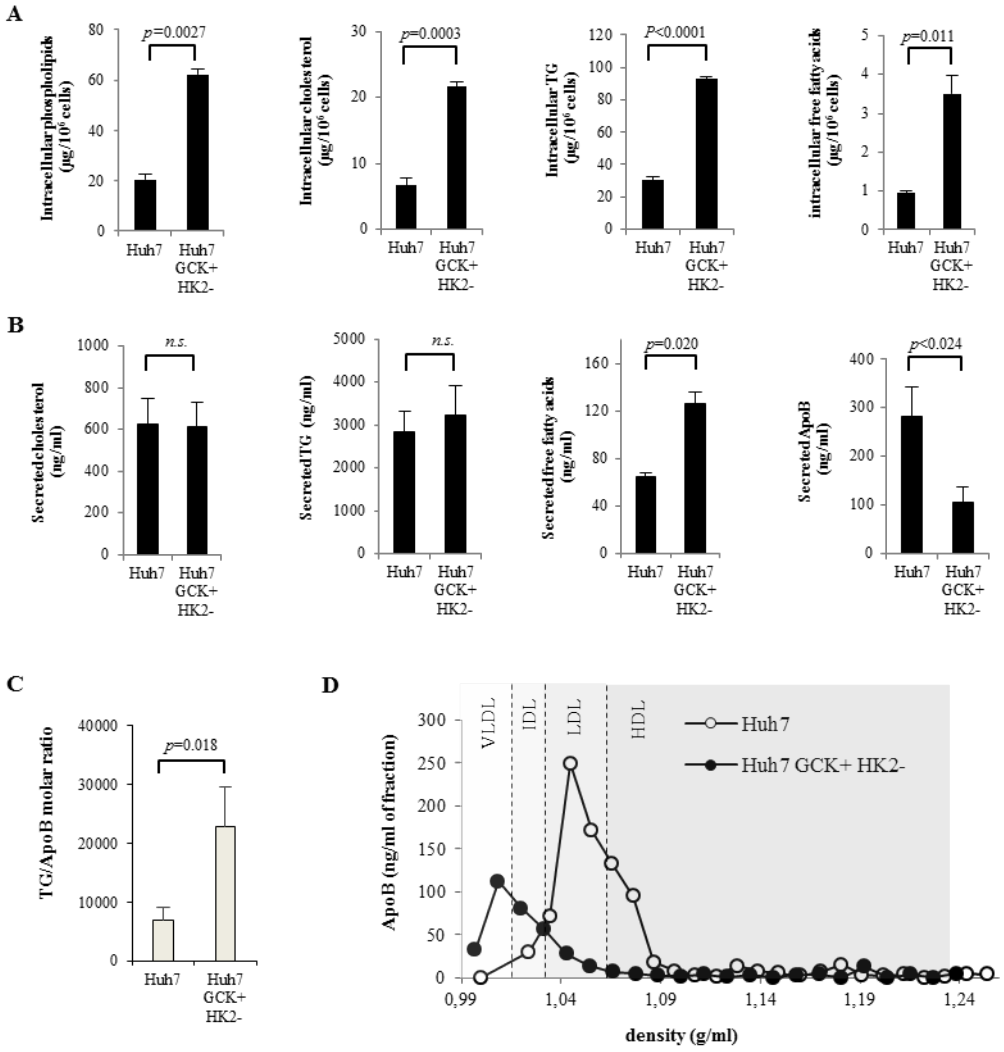

Figure 4

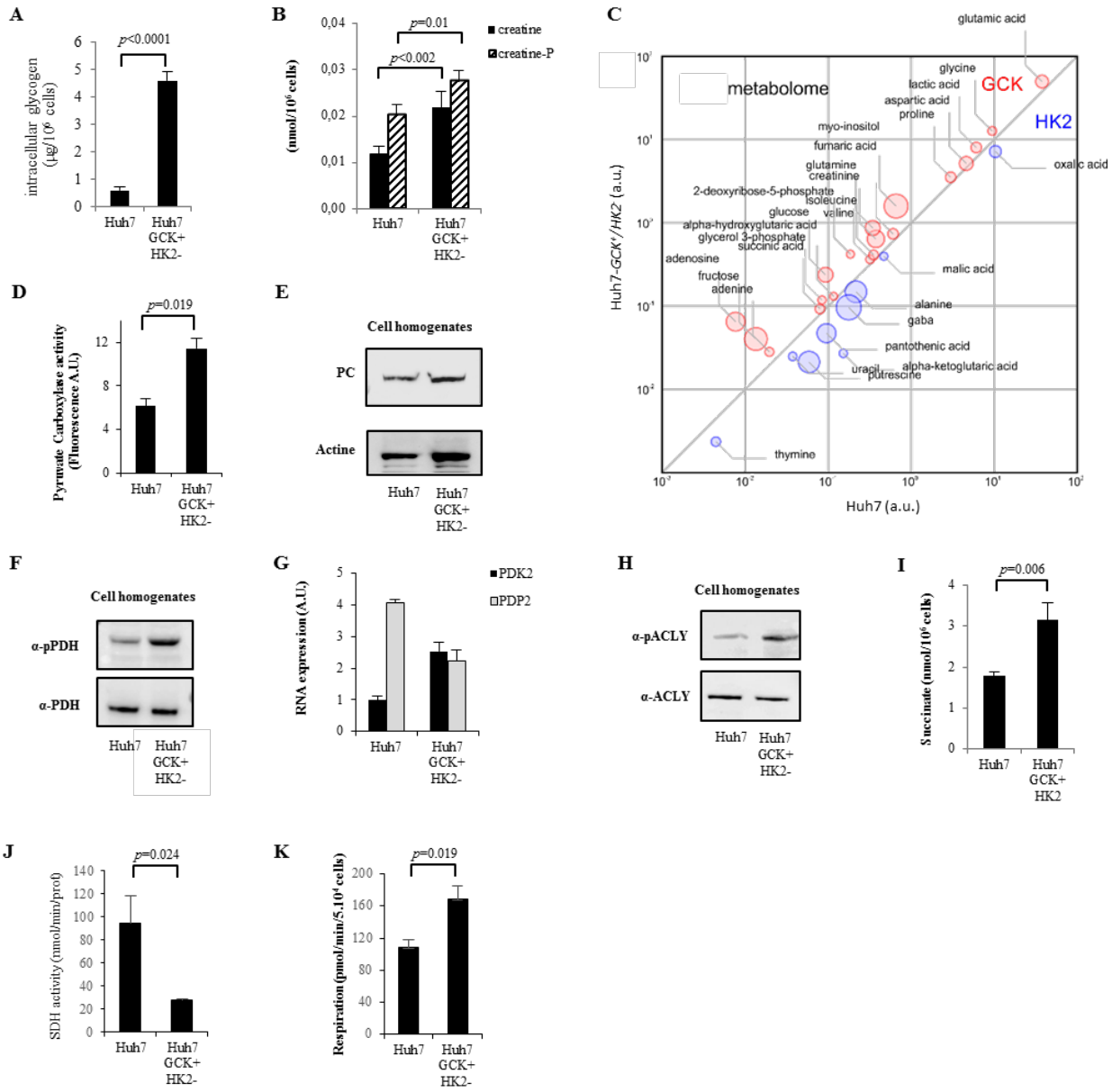

Figure 5

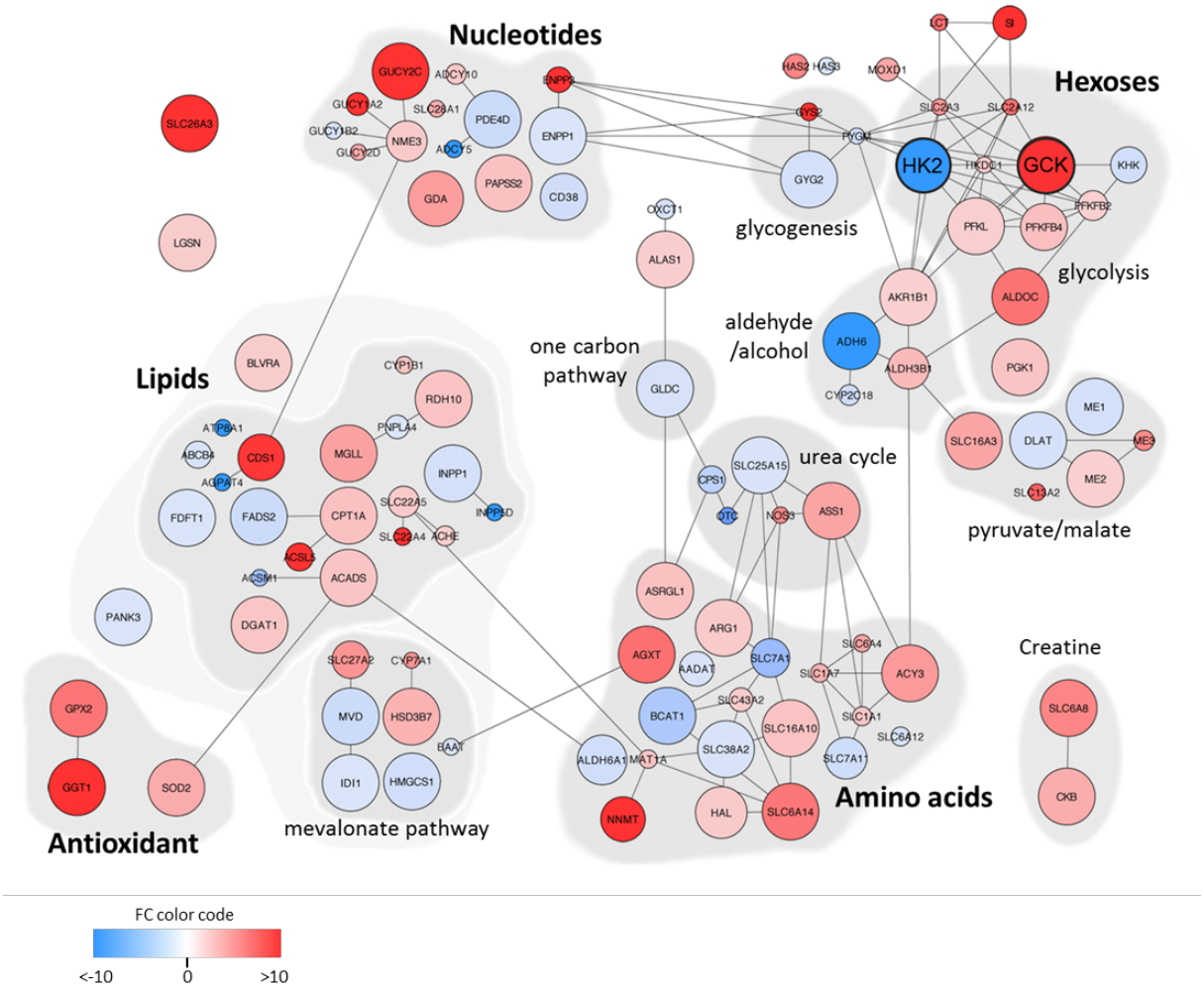

Figure 6

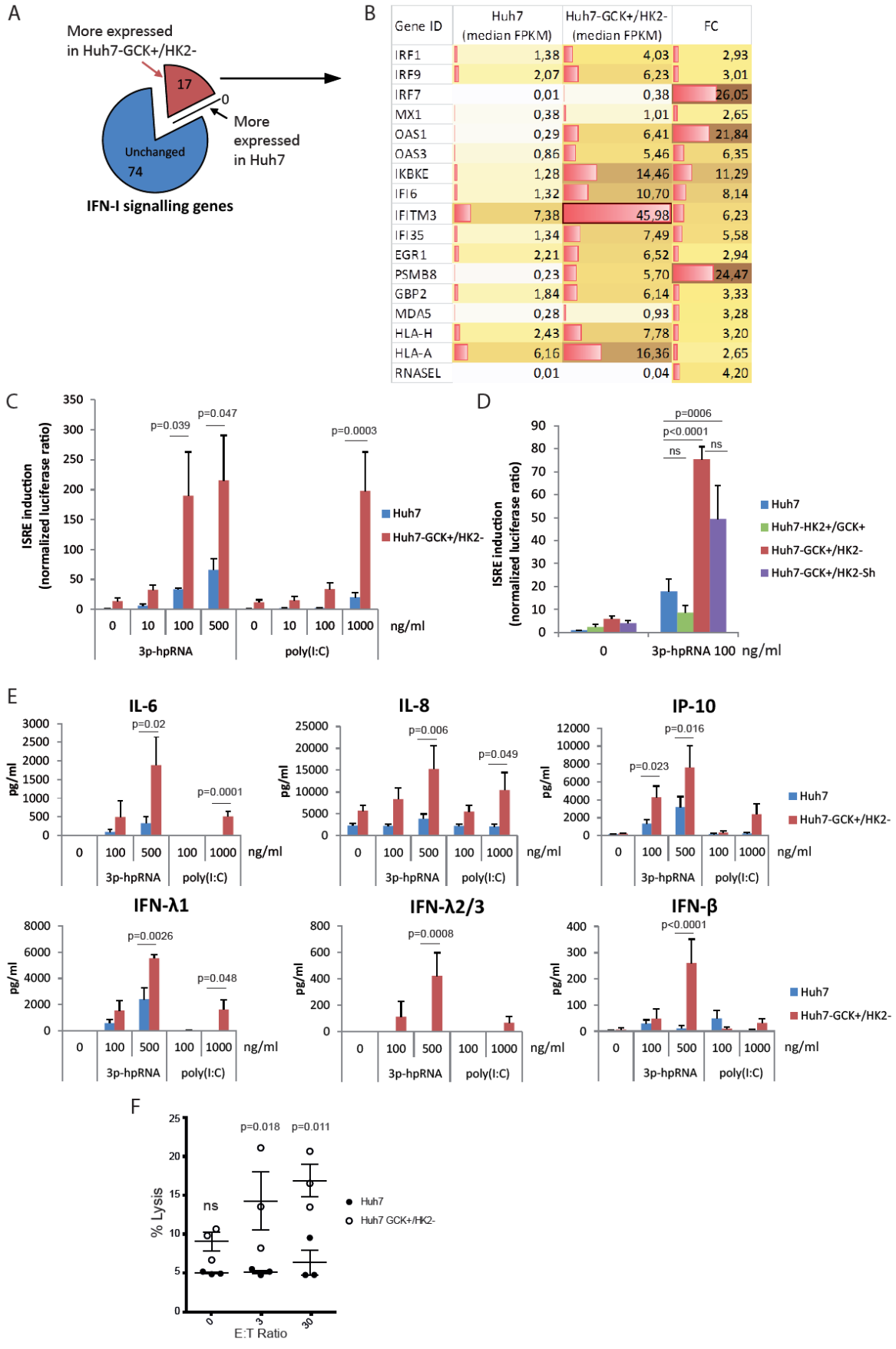

Gene ID	Huh7 (median FPKM)	Huh7-GCK+/HK2- (median FPKM)	FC
IRF1	1,38	4,03	2,93
IRF9	2,07	6,23	3,01
IRF7	0,01	0,38	26,05
MX1	0,38	1,01	2,65
OAS1	0,29	6,41	21,84
OAS3	0,86	5,46	6,35
IKBKE	1,28	14,46	11,29
IFI6	1,32	10,70	8,14
IFITM3	7,38	45,98	6,23
IFI35	1,34	7,49	5,58
EGR1	2,21	6,52	2,94
PSMB8	0,23	5,70	24,47
GBP2	1,84	6,14	3,33
MDA5	0,28	0,93	3,28
HLA-H	2,43	7,78	3,20
HLA-A	6,16	16,36	2,65
RNASEL	0,01	0,04	4,20

Figure 7